Influence of PMSM Parameters on the Active Open- vs Short-Circuit Fault-Reaction Strategy

(Article begins on next page)

Influence of PMSM Parameters on the Active Open- vs Short-Circuit Fault-Reaction Strategy

Simone Ferrari
Energy Department "Galileo Ferraris"
Politecnico di Torino
Turin, Italy
simone.ferrari@polito.it

Paolo Pescetto
Energy Department "Galileo Ferraris"
Politecnico di Torino
Turin, Italy
paolo.pescetto@polito.it

Gianmario Pellegrino
Energy Department "Galileo Ferraris"
Politecnico di Torino
Turin, Italy
gianmario.pellegrino@polito.it

***Abstract*—Defining the Fault-Reaction Strategy (FRS) is crucial for Permanent Magnet Synchronous Machines (PMSMs). In general, two approaches can be adopted: Active Open-Circuit (AOC) and Active Short-Circuit (ASC), with pros and cons. The former is safer for the motor, as high demagnetizing current are avoided, but can lead to undesired and dangerous voltages. The latter limit voltages effectively, but induces high currents that can irreversibly demagnetize the motor and stress the converter components. This paper proposes a unified framework to compare AOC and ASC by linking them to key PMSM parameters (anisotropy and PM flux linkage), through both Constant Parameter Model (CPM) and Finite Element Analysis (FEA). Furthermore, a mixed AOC+ASC strategy is proposed to simultaneously mitigate currents and avoid overvoltages. The scheme is related to the PMSM parameters and it is validated on four machines, with different saliency ratios and PM strengths, highlighting the impact of saturation and temperature on the final FRS decision.**

***Index Terms*—Permanent Magnet Synchronous Machines, Active Short-Circuit, Demagnetization, Fault Reaction**

I. Introduction

Permanent Magnet Synchronous Machines (PMSMs) are widely adopted in several sectors, thanks to the high power density and the wide achievable Constant Power Speed Range (CPSR). Despite their popularity, defining robust Fault-Reaction Strategies (FRSs) for PMSMs remains a critical challenge. The simplest FRS is the Active Open-Circuit (AOC), which turns off the power converter and get rid of current flow. However, it can be unsuitable for safety-critical systems if the resulting no-load voltage exceeds the DC-link limit. This condition, called Uncontrolled Generator Operation (UGO), can damage the inverter and the battery and posing a danger for users. To avoid overvoltages, many applications adopt Active Short-Circuit (ASC) instead. This is the standard in the automotive sector [1]–[3] as it is inherently safe against high voltages. Its use is also spreading in aerospace [4] and industrial drives [5]. Nonetheless, ASC induces high currents, that can demagnetize the Permanent Magnets (PMs), especially if ferrite PMs are adopted [6]–[8], and it increases stress on power converters. Hence, a clear understanding of the ASC and AOC behaviors, as function of the machine parameters, is imperative, both at the early PMSM design stage, and when implementing the FRS on the final design.

The aim of this paper is twofold. First, it introduces dedicated metrics for assessing AOC and ASC as function of the main PMSM parameters, namely the anisotropy ratio ξ and the p.u. PM flux linkage $\frac{\lambda_m}{\lambda_{max}}$. Second, it proposes and formalize a mixed AOC+ASC strategy that address the limitations of both FRSs. The analysis will be developed both on real machines, through accurate Finite Element Analysis (FEA) simulations, and with Constant Parameter Model (CPM) which, though less presice, offer deeper analytical insights and ease the general understanding.

A. Benchmark Motors

To demonstrate the FRS analysis methodology and evaluate the CPM's accuracy, four benchmark machines are considered:

- a traction Interior PM (IPM) machine with NdFeB magnets, serving as the primary benchmark;
- a PM-assisted Synchronous Reluctance (PM-SyR) machine with NdFeB magnets
- a pure Synchronous Reluctance (SyR) machine
- a Surface-mounted PM (SPM) machine

Their key ratings are summarized in Tab. I, while Fig. 1 shows their cross-sections. All machine models are parametrized in SyR-e [9] for consistent, repeatable analysis.

II. Machine Model

The steady-state model of a generic PMSM can be expressed as:

$$v_{dq} = R_s \cdot i_{dq} + j \cdot \omega \cdot \lambda_{dq} \tag{1}$$

where v_{dq} is the phase voltage in dq components, R_s is the phase stator resistance, i_{dq} is the phase current in dq

TABLE I
Benchmark Machines Ratings

		IPM	PM-SyR	SyR	SPM
Peak current	(A)	800	42	30	30
DC-link voltage	(V)	400	310	565	565
Peak torque	(Nm)	460	44	41	61
Peak power	(kW)	224	11	11	14
Base speed	(rpm)	4300	2100	2400	2200
Maximum speed	(rpm)	18000	9000	6000	3000
Stator outer diameter	(mm)	225	170	175	175
Stack length	(mm)	134	115	110	110

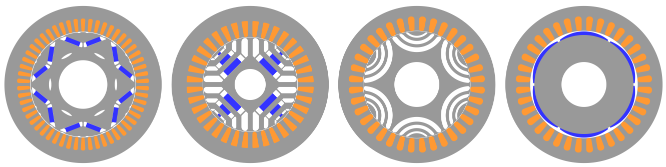

(a) (b) (c) (d)

Fig. 1. Cross sections of the four benchmark machines: (a) IPM, (b) PM-SyR, (c) SyR and (d) SPM.

components, j is the imaginary operator, ω is the electric pulsation and λ_{dq} is the dq flux linkage. Usually, λ_{dq} are expressed via two-dimensional flux maps, defined as:

$$\begin{cases} \lambda_d = \mathbf{\Lambda}_d(i_d, i_q) \\ \lambda_q = \mathbf{\Lambda}_q(i_d, i_q) \end{cases} \tag{2}$$

Here, the bold-font symbols $\mathbf{\Lambda}_d$ and $\mathbf{\Lambda}_q$ emphasize that flux linkages are functions of both i_d and i_q. Despite these strong non-linearities, a Constant Parameter Model (CPM) is often used to gain deeper insight into core machine behaviors and simplify the theoretical explanation of some computations. Under CPM, flux linkages are expressed as:

$$\begin{cases} \lambda_d &= L_d \cdot i_d + \lambda_m \\ \lambda_q &= L_q \cdot i_q \end{cases} \tag{3}$$

where L_d and L_q are the dq inductances and λ_m is the PM flux linkage. The torque can be computed as:

$$T = \frac{3}{2} \cdot p \cdot (\lambda_d \cdot i_q - \lambda_q \cdot i_d) \tag{4}$$

where p is the pole pairs number. The approach of flux maps can be extended to torque, with the computation of the torque map $\mathbf{T}$.

To determine actual machine performance, optimal control trajectories, namely Maximum Torque per Ampere (MTPA) and Maximum Torque per Volt (MTPV), must be considered. These trajectories can be easily computed from flux and torque maps [9]. Furthermore, inverter constraints must be accounted for. These are the maximum phase current I_{max} and the DC link voltage V_{DC}.

Fig. 2 shows the torque-speed and power-speed profiles of the IPM benchmark under its inverter limits and in lossless conditions. At low speed, the motor is controlled along the MTPA, expressing the maximum flux linkage λ_{max}. This happens until the voltage saturates at the base speed n_{base} is reached. Beyond this speed, field-weakening is implemented, first rotating the current vector and, from n_{MTPV}, reducing the current, according the MTPV curve. Another key speed is n_{CPSR}, related to the Constant Power Speed Range (CPSR) and defined as the maximum speed at which the machine can still produce its rated (base) power.

A good index of the CPSR (and a good field-weakening capability) is the characteristic current i_{ch} [10], expressed as:

$$\lambda_d(-i_{ch}, 0) = 0 \tag{5}$$

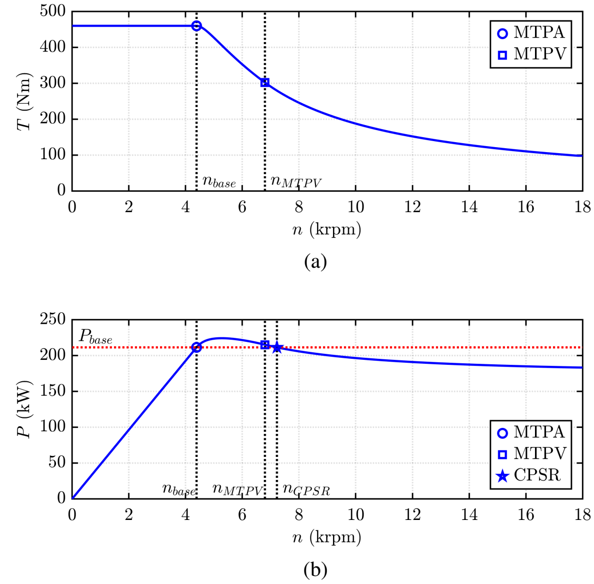

Fig. 2. Torque and power profiles at maximum current and voltage in loss-less condition.

This is the current needed to counteract the PM flux linkage such that the total net flux linkage becomes zero. Under CPM, i_{ch} is expressed as:

$$i_{ch} = \frac{\lambda_m}{L_d} \tag{6}$$

As i_{ch} is the current asymptote at infinite speed, its value is related to the power at maximum speed of the machine.

A. Parametric PMSM Plane

The parametric PMSM plane, firstly introduced in [10], [11], reports per-unit machine performance figures function of the anisotropy factor $\xi = \frac{L_q}{L_d}$ and the per-unit flux linkage $\frac{\lambda_m}{\lambda_{max}}$, under the assumption of CPM. In this way, several types of PMSM are covered, ranging from SPM machines ($\lambda_m \approx \lambda_{max}$ and $\xi \approx 1$) to SyR machines ($\lambda_m = 0$ and $\xi \gg 1$), as well as IPM and PM-SyR machines with intermediate saliency and magnet flux.

Fig. 3 illustrates two example metrics on this plane: the CPSR defined as $\frac{n_{CPSR}}{n_{base}}$ and the per-unit characteristic current

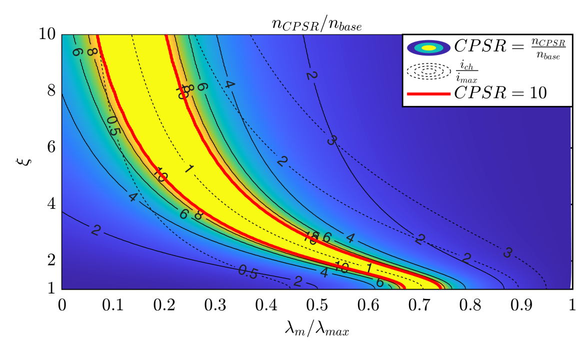

Fig. 3. Per-unit characteristic current and CPSR reported on the parametric PMSM plane

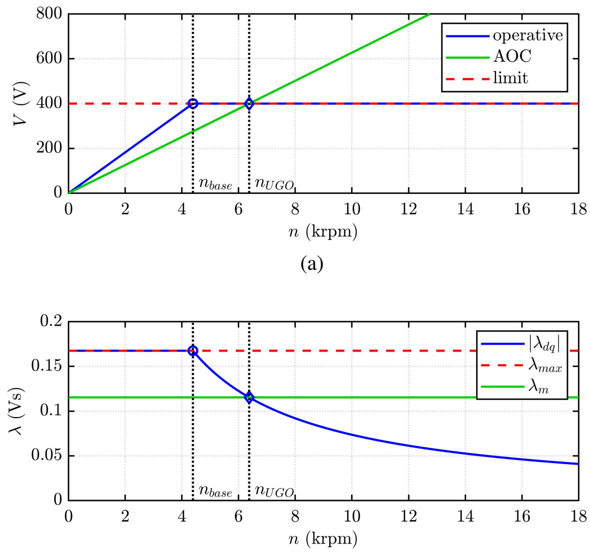

Fig. 4. Identification of the UGO speed limit during AOC: a) voltage versus speed and b) flux linkage versus speed.

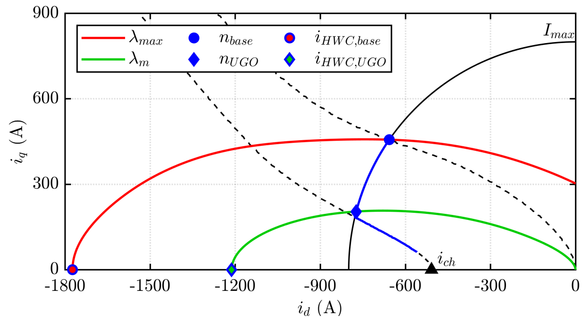

Fig. 5. Graphical identification of the peak current during ASC, based on the pre-fault condition.

$\frac{i_{ch}}{I_{max}}$. According to [10], CPSR tends to ∞ when $\frac{i_{ch}}{I_{max}} \simeq 1$. The contours at $\frac{n_{CPSR}}{n_{base}} = 10$ are reported in red and will be used as reference in the following. Although this framework is based on CPM, omitting saturation and other nonlinear effects, it offers valuable insight into how fundamental parameters influence PMSM output and will be the base for the following FRS analysis.

III. Fault-Reaction Strategies Definition

A. Active Open-Circuit

During AOC, the inverter modulation is disabled, forcing the phase current to zero and making the inverter effectively passive. The main issue with AOC is the Uncontrolled Generator Operation (UGO), which occurs when the motor's back-emf exceeds the DC-link voltage. This risk is particularly relevant for PMSMs with wide CPSR, where deep field-weakening is adopted.

Fig. 4 illustrates this issue. In Fig. 4a, the line voltage of the benchmark IPM machine is plotted versus speed under two different conditions: operating at maximum current (blue) and running at no-load (green). In normal operation, the voltage increases up to the base speed, where it reaches the inverter limit. From this speed on, field-weakening reduces the machine flux linkage λ_{dq} in proportion to speed, as shown in Fig. 4b, keeping the voltage constant with speed. Meanwhile, the green curves in Fig. 4a shows how voltage in AOC grows with a slope determined by the PM flux linkage λ_m (reported in green in Fig. 4b). The UGO speed n_{UGO} is where this no-load voltage meets the voltage limit, or when the PM flux linkage equals the operating flux linkage amplitude.

Neglecting the phase resistance R_s, the UGO limit n_{UGO} can be derived from (1) applied to operating and AOC conditions at base and UGO limit speed, respectively, resulting in:

$$n_{UGO} = n_{base} \cdot \left(\frac{\lambda_m}{\lambda_{max}} \right)^{-1} \tag{7}$$

Accordingly, AOC is safe only if triggered at speeds not exceeding n_{UGO}.

B. Active Short-Circuit

The other FRS, typically adopted in the automotive sector, is the ASC, in which the inverter phases short-circuit the motor terminals. This removes the dangerous open-circuit voltage but can produce large fault currents, with the risks of irreversible PMs demagnetization, inverter damage, and excessive heating if sustained for long durations.

A simple measure of ASC severity is the steady-state short-circuit current, which, for negligible R_s and at high speed, tends toward the characteristic current (5). However, the transient peak can be much higher, necessitating more detailed analysis. This work adopts the Hyper-Worst-Case (HWC) current concept from [12], which identifies the maximum theoretical short-circuit current based on flux maps and in loss-less condition. Without losses, the flux linkage amplitude remains constant during the fault, and the peak current occurs when aligned against the PM flux linkage.

Two main pre-fault operating points are considered: base speed n_{base}, where the flux linkage is at its maximum ($|\lambda_{dq}| = \lambda_{max}$) and the UGO limit speed n_{UGO}, where $|\lambda_{dq}| = \lambda_m$. Accordingly, the HWC current values are computed by:

$$\mathbf{\Lambda}_d(-i_{HWC,base}, 0) = -\lambda_{max} \tag{8}$$

$$\mathbf{\Lambda}_d(-i_{HWC,UGO}, 0) = -\lambda_m \tag{9}$$

Fig. 5 graphically illustrates how these HWC currents are identified on the (i_d, i_q) plane for each pre-fault point. The flux linkage contours $|\lambda_{dq}| = \lambda_{max}$ (red) and $|\lambda_{dq}| = \lambda_m$ (green) are the flux linkages at n_{base} and n_{UGO}, respectively (reported with blue circle and diamond). The corresponding HWC currents are identified intersecting these iso-flux-linkage contours with the $-d$ axis, as highlighted with colored markers.

Under the CPM, these HWC currents can be estimated analytically. At base speed, (8) becomes:

$$L_d \cdot (-i_{HWC,base}) + \lambda_m = -\lambda_{max} \tag{10}$$

and after some math, the HWC current reached from base speed results in:

$$i_{HWC,base} = \frac{\lambda_{max} + \lambda_m}{L_d} = i_{ch} \cdot \left[1 + \left(\frac{\lambda_m}{\lambda_{max}}\right)^{-1}\right] \tag{11}$$

This confirms that the peak current during ASC is higher than the steady-state value (that is i_{ch}). Furthermore, for PMSMs with smaller λ_m (and typically high ξ), the current overshoot is magnified due to the term $1 + \left(\frac{\lambda_m}{\lambda_{max}}\right)^{-1}$.

If ASC is triggered at n_{UGO}, the CPM yields:

$$L_d \cdot (-i_{HWC,UGO}) + \lambda_m = -\lambda_m \tag{12}$$

and highlighting the HWC current, the equation becomes:

$$i_{HWC,UGO} = 2 \cdot i_{ch} \tag{13}$$

Thus, under CPM assumptions, the peak current from the UGO-speed condition is always twice the characteristic current, independent of other machine parameters.

C. Mixed AOC+ASC Strategy

From the above discussion, neither pure AOC nor pure ASC is safe for the complete speed range. Below n_{UGO}, AOC is safe and avoids high current peaks. Above n_{UGO}, however, AOC becomes unsafe (due to excessive voltage), making ASC necessary. Crucially, at these higher speeds the machine is in a field-weakening region, so the short-circuit current is limited, compared to a pure ASC strategy, as highlighted in the previous section.

Fig. 6 illustrates this mixed AOC+ASC FRS for the benchmark IPM machine. The green region shows speeds where AOC can be adopted without violating the voltage limit, while the orange area highlights the speed region requiring ASC to prevent overvoltage. Compared to using only AOC or only ASC, this hybrid approach constrains both voltage and current to safer levels. In the example, the pure-AOC case leads to unsafe voltage for most of the speed range, as n_{UGO} is about 35% of the maximum speed. Whereas, the pure ASC case induce peak currents of 1774 A. By implementing the AOC+ASC strategy and triggering ASC for speeds higher than n_{UGO}, the short-circuit current is reduced to 1210 A (-32%), mitigating the stress on the inverter and the demagnetization risk.

D. FRS Metrics on the Parametric PMSM Plane

For a broader perspective, these FRS metrics can be mapped onto the parametric PMSM plane introduced in Fig. 3. Fig. 7 reports the AOC metric n_{UGO}/n_{base} and the ASC metrics $\frac{i_{ch}}{I_{max}}$, $\frac{i_{HWC,base}}{I_{max}}$ and $\frac{i_{HWC,UGO}}{I_{max}}$. The red curves again reference $\frac{n_{CPSR}}{n_{base}} = 10$.

From Fig. 7a, it is evident that AOC poses fewer problems for machines with lower $\frac{\lambda_m}{\lambda_{max}}$. Highly anisotropic machines

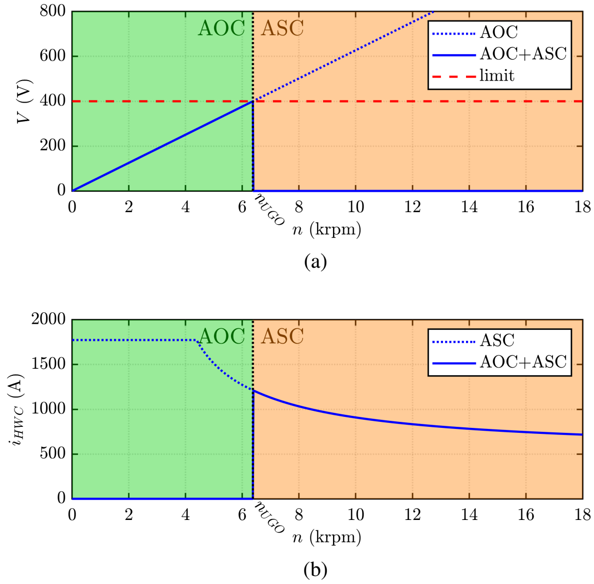

Fig. 6. Mixed AOC+ASC strategy: (a) no-load voltage and (b) HWC current function of the machine speed.

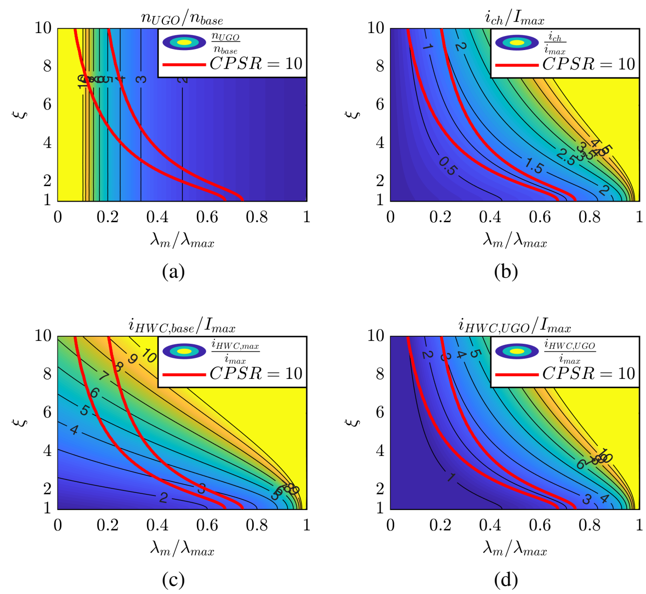

Fig. 7. FRS indices on the parametric PMSM plane, expressed in per-unit: (a) UGO speed limit, (b) characteristic current, (c) HWC current from base speed and (d) HWC current from UGO speed.

also benefit from higher UGO limits, that is also compatible with the wider field-weakening region (typical of PM-SyR designs). Meanwhile, SPM machines tend to have $n_{UGO} \simeq n_{base}$, but as the field-weakening is not implemented for these machines, UGO issues are typically avoided.

Focusing on ASC indices, the peak current can reach several times I_{max}. For SPM machines, HWC current is high because of the high $\frac{i_{ch}}{I_{max}}$ ratio. Conversely, PM-SyR machines can reach high HWC current because of the unfavorable $1 + \left(\frac{\lambda_m}{\lambda_{max}}\right)^{-1}$ factor, that strongly magnify i_{ch}. Obviously, the intermediate $\left(\xi, \frac{\lambda_m}{\lambda_{max}}\right)$ combinations presents a mix of the two conditions.

The high ASC current can be limited by the AOC+ASC FRS, especially for PM-SyR machines. Typically these machines are equipped with weak ferrite PMs, sensitive to demagnetization and for which the short-circuit current must be limited as much as possible, but the ASC current from n_{base} is high and increased by the $1+\left(\frac{\lambda_m}{\lambda_{max}}\right)^{-1}$ factor. However, if the ASC is triggered from n_{UGO} (way higher than n_{base}), the ASC current is reduced to $i_{HWC,UGO} = 2 \cdot i_{ch}$ (with CPM assumption), allowing a safe ASC maneuvre. Furthermore, for these machines, i_{ch} is reduced, because of the low PM content, resulting in fault currents comparable with the maximum machine current.

IV. Real Machines Assessment

This section examines how real machine behaviors affect the fault-reaction (FRS) metrics defined earlier.

A. Effect of Iron Saturation

The first aspect considered is the machine's non-linear magnetic behavior. Although the CPM offers deep insights on PMSMs behaviors, its accuracy is limited by iron saturation. To assess its impact, the CPM parameters are computed from FEA-simulated flux maps (2), according to the apparent inductance formulation:

$$\begin{cases} \mathbf{\Lambda}_m(i_d, i_q) & = \mathbf{\Lambda}_d(0, i_q) \\ \mathbf{L}_d(i_d, i_q) & = (\mathbf{\Lambda}_d - \mathbf{\Lambda}_m) \oslash \mathbf{I}_d \\ \mathbf{L}_q(i_d, i_q) & = \mathbf{\Lambda_q} \oslash \mathbf{I}_q \end{cases} \tag{14}$$

where the symbol $\oslash$ represents the element-wise division. Because of iron saturation, both ξ and $\frac{\lambda_m}{\lambda_{max}}$ are variable along the operating speed range. Fig. 8 shows the parametric PMSM plane with the four benchmark motors highlighted with different colors. Each machine is represented by a "cloud of point", as L_d, L_q and λ_m change over the operating range. As this analysis deals just with full-current performance, the "cloud of points" collapsed in a single curve, representative of the maximum torque per speed curve. The base speed and UGO limit speed points are highlighted with circle and diamond marker, respectively.

As expected, iron saturation alters the machine's parameters, giving to the PMSM plane the role of an insightful but qualitative tool. IPM and PM-SyR machines show larger parameter variations, with a deep change of the $\left(\xi, \frac{\lambda_m}{\lambda_{max}}\right)$ point, while SPM machine parameters are more constant, thanks to its limited field-weakening range.

The per-unit metrics are extracted from the plane for each machine at base and UGO limit speeds and reported in Tab. II, together with the results obtained by FEA-computed magnetic model. The overall accuracy is limited, as discussed before. The UGO limit speed is better estimated if the parameters are retrieved at this speed, while ASC currents are more accurate if the parameters are retrieved at base speed. The main source of error is the saturation, that change the maximum flux linkage value, given the maximum current CPM parameters.

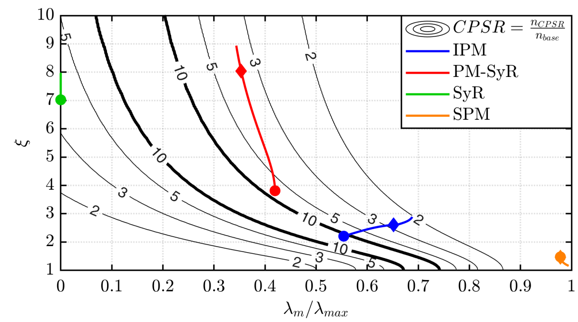

Fig. 8. PMSM parametric plane with the coordinates of the four benchmark motors, computed accounting for saturation. Circles are the base speed points and diamonds are the UGO speed limit.

TABLE II
CPM Validation

	IPM			PM-SyR			SyR			SPM		
	FEA	CPM base	CPM UGO	FEA	CPM base	CPM UGO	FEA	CPM base	CPM UGO	FEA	CPM base	CPM UGO
$\frac{\lambda_m}{\lambda_{max}}$	-	0.55	0.65	-	0.42	0.36	-	0.00	-	-	0.98	0.98
ξ	-	2.21	2.61	-	3.77	8.08	-	7.02	-	-	1.47	1.46
$\frac{i_{ch}}{I_{max}}$	0.64	1.10	1.66	0.97	1.30	2.32	0.00	0.00	-	3.42	5.21	5.19
$\frac{i_{HWC,base}}{I_{max}}$	2.22	3.07	4.21	5.45	4.40	8.82	4.45	5.02	-	7.46	10.54	10.50
$\frac{i_{HWC,UGO}}{I_{max}}$	1.52	2.19	3.32	2.27	2.61	4.65	-	-	-	7.43	10.42	10.38
$\frac{i_{HWC,base}}{i_{ch}}$	3.49	2.81	2.53	5.64	3.38	3.80	-	-	-	2.18	2.02	2.02
$\frac{i_{HWC,UGO}}{i_{ch}}$	2.39	2.00	2.00	2.34	2.00	2.00	-	-	-	2.17	2.00	2.00
$\frac{n_{CPSR}}{n_{base}}$	1.65	14.25	2.71	∞	7.09	3.44	1.69	3.58	-	1.09	1.09	1.08
$\frac{n_{UGO}}{n_{base}}$	1.45	1.81	1.53	2.95	2.38	2.80	∞	∞	-	1.01	1.02	1.02

As an example, Fig. 9a shows the flux linkage versus speed for the IPM machine benchmark; the CPM overestimates λ_{max}, mainly due to neglecting saturation. This misestimate is evident also from the lower current angle along the maximum torque per speed curve, reported in Fig. 9b, that false the base speed (i_d, i_q) operating point. Despite this discrepancy, the resulting HWC currents and n_{UGO} predictions remain reasonably accurate for all the considered benchmark. The former because in HWC condition the machine is deeply saturated, with almost constant inductances; and the latter because at n_{UGO}, the flux linkage is limited, avoiding uneaven saturation effects. Notably, $\frac{i_{HWC,UGO}}{i_{ch}}$ remains near 2.0, matching the theoretical relation in (13).

B. Effect of PM Temperature

Temperature effects are next considered using the IPM benchmark and FEA-computed model, computed at three PM temperatures (20°C, 80°C and 120°C). Increased magnet temperature Θ_{PM} lowers the PM remanence, hence reducing λ_m and modifying the flux maps, while also decreasing the demagnetization limit I_{demag}, that is the ultimate HWC current limit to consider safe the ASC. Fig. 10a reports the torque-speed limits at each temperature. Although the torque curves differ marginally, n_{UGO} increases with temperature due to the lower λ_m. The gray-shaded area highlight highlights the UGO limit speed variation with Θ_{PM}. Consequently, the HWC current at n_{UGO} can be slightly higher at low temperatures (since λ_m is larger). However, the dominant variation with Θ_{PM} is on

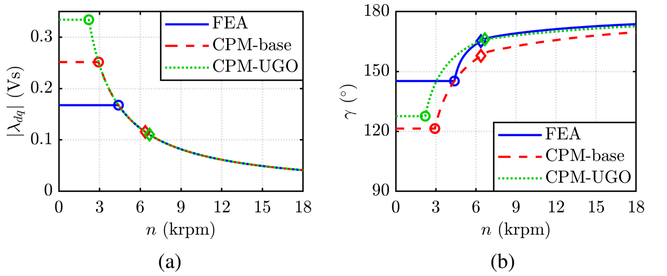

Fig. 9. Effect of iron saturation on (a) power and (b) flux linkage versus speed. Comparison between FEA model and CPM computed at base and UGO speed.

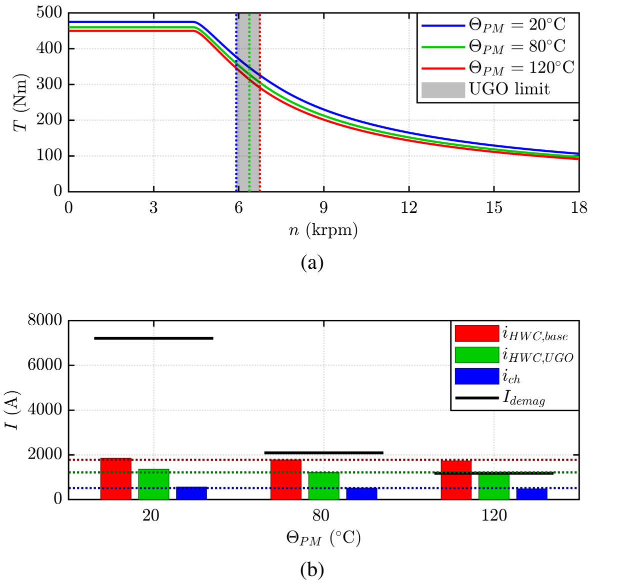

Fig. 10. Effect of PM temperature: (a) torque versus speed limit with UGO speed highlighted and (b) HWC current and demagnetization limit.

the demagnetization limit I_{demag}, which drops significantly at higher Θ_{PM}, as reported in Fig. 10b. The figures includes also HWC and characteristic currents, demonstrating that the temperature effects on the latter is limited. This results in a reduced safety margin with temperature increase. It is worth noting that at 120°C, triggering ASC at n_{base} would exceed I_{demag}, but switching ASC at n_{UGO} remains safe. This highlights the importance of a mixed AOC+ASC approach at elevated temperatures.

V. Conclusions

This paper presented a comprehensive analysis on fault reaction strategies for PMSM, across various machine types. The analysis starts with a simplified CPM framework, illustrating how PM flux linkage and anisotropy affect AOC and ASC metrics. These indices are mapped on the parametric PMSM plane, providing a clear, graphical insight into how flux linkage and anisotropy influence the choice of FRS. Building on these results, a mixed AOC+ASC strategy is formalized. In this approach, AOC is applied below the UGO speed limit and ASC above it, thus avoiding dangerous overvoltages and limiting the ASC peak current to twice the characteristic current. This hybrid method is particularly advantageous for PMSMs with a wide CPSR (i.e. deep field-weakening operations) and yields the greatest benefits in PM-SyR machines with weak ferrite magnets, that can preserve magnet integrity. Although CPM approach provides strong insight, it remains qualitative, as non-linear machine behaviors are neglected. However, the analytical methodology proposed for FRS metrics computation can be extended to non-linear models, enabling the easy definition of the proper FRS with realistic machine. This was tested on four actual benchmarks. Ultimately, the AOC+ASC approach still proves effective in reducing demagnetizing currents and maintaining safe voltage and current levels across the full operating range.

Acknowledgment

The research has been conducted with the support of Power Electronics Innovation Center (PEIC) of Politecnico di Torino.

References

[1] ISO/TC 22/SC 32, "ISO26262-1:2018." International Organization for Standardization, 2018. [Online]. Available: https://www.iso.org/standard/68383.html

[2] S. Chen, X. Hao, C. Gao, and Z. Jiang, "An Effective Nontransient Active Short-Circuit Method for PMSM in Electric Vehicles," *IEEE Transactions on Industrial Electronics*, vol. 70, no. 4, pp. 3571–3580, Apr. 2023.

[3] G. Choi and T. M. Jahns, "Investigation of Key Factors Influencing the Response of Permanent Magnet Synchronous Machines to Three-Phase Symmetrical Short-Circuit Faults," *IEEE Transactions on Energy Conversion*, vol. 31, no. 4, pp. 1488–1497, Dec. 2016.

[4] W. Wang, J. K. Nøland, P. K. Olsen, and S. W. Johannessen, "Optimal Active Short-Circuit Operation of Permanent Magnet Synchronous Machines and Drives for Aerospace Applications," in *2024 International Conference on Electrical Machines (ICEM)*, Torino, Italy, Sep. 2024, pp. 1–7.

[5] B. Jung, W. Lee, J. Choi, and Y. Kim, "Active Short Circuit Method for Reducing Short-Current in Air Conditioning Systems," *IEEE Transactions on Industry Applications*, pp. 1–10, 2025.

[6] R. Leuzzi, P. Cagnetta, F. Cupertino, S. Ferrari, and G. Pellegrino, "Performance assessment of ferrite- and neodymiumassisted synchronous reluctance machines," in *2017 IEEE Energy Conversion Congress and Exposition (ECCE)*, Oct. 2017, pp. 3958–3965.

[7] M.-J. Jeong, H.-J. Pyo, D.-W. Nam, S.-H. Yang, K. Lee, and W.-H. Kim, "The Study on Improving Reluctance Torque and Preventing Irreversible Demagnetization by Modified the Shape of Conventional Ferrite Flux-Concentrated Motor," in *2020 IEEE Energy Conversion Congress and Exposition (ECCE)*, Detroit, MI, USA, Oct. 2020, pp. 1386–1391.

[8] D. Yun Kwon, K. W. Kim, T. H. Kwon, and M. Jeong, "Research on Design and Electromagnetic Characteristics Analysis of Super Premium Efficiency (IE4) Permanent Magnet Assisted Synchronous Reluctance Motor for Rare Earth Permanent Magnet Reduction," in *2024 27th International Conference on Electrical Machines and Systems (ICEMS)*, Fukuoka, Japan, Nov. 2024, pp. 1118–1121.

[9] Simone Ferrari and Gianmario Pellegrino, "SyR-e/syre_public: SyR-e v3.8.2," Oct. 2024. [Online]. Available: www.github.com/SyR-e

[10] D. Staton, W. Soong, R. Deodhar, and T. Miller, "Unified theory of torque production in ac, dc and reluctance motors," in *Proceedings of 1994 IEEE Industry Applications Society Annual Meeting*, vol. 1, 1994, pp. 149–156 vol.1.

[11] W. Soong and N. Ertugrul, "Field-weakening performance of interior permanent-magnet motors," *IEEE Transactions on Industry Applications*, vol. 38, no. 5, pp. 1251–1258, Sep. 2002.

[12] S. Ferrari, G. Dilevrano, P. Ragazzo, P. Pescetto, and G. Pellegrino, "Fast determination of transient short-circuit current of pm synchronous machines via magnetostatic flux maps," *IEEE Transactions on Industry Applications*, vol. 59, no. 4, pp. 4000–4009, 2023.